Structure resolution by electron diffraction tomography of the complex layered iron-rich Fe-2234-type Sr 5 Fe 6 O 15.4

Christophe Lepoittevin

Structure resolution by Electron Diffraction Tomography of the complex layered Iron-Rich Fe-2234-type $Sr_5Fe_6O_{15.4}$

Christophe Lepoittevin[a,]*

[a]*Univ. Grenoble Alpes, CNRS, Institut NEEL, 25 Avenue des Martyrs, B.P. 166, F-38042 Grenoble, France.*

*Corresponding author at: Univ. Grenoble Alpes, CNRS, Institut NEEL, 25 Avenue des Martyrs, B.P. 166, F-38042 Grenoble, France.
E-mail address: christophe.lepoittevin@neel.cnrs.fr

A B S T R A C T

The crystal structure of the strontium ferrite $Sr_5Fe_6O_{15.4}$, was solved by direct methods on electron diffraction tomography data acquired on a transmission electron microscope. The refined cell parameters are a = 27.4047(3) Å, b = 5.48590(7) Å and c = 42.7442(4) Å in *Fm2m* symmetry. Its structure is built up from the intergrowth sequence between a quadruple perovskite-type layer with a complex rock-salt (RS)-type block. In the latter iron atoms are found in two different environments : tetragonal pyramid and tetrahedron. The structural model was refined by Rietveld method based on the powder X-ray diffraction pattern.

Keywords :
Electron diffraction tomography
Complex strontium iron based structure
Powder X-ray diffraction

1. Introduction

In the search for new high Tc superconducting materials (HTSC), large structural families have been found out. They are characterized by *n* rock-salt (RS) type layers (*n* = 1, *n* = 2 or *n* = 3) and *m* perovskite-type layers. In the Sr-A-O system (A = 3d transition element), the RS block consists of (*n* - 1) intermediate [AO] layer(s) sandwiched between two [SrO] layers, and the perovskite block is made of (*m* - 1) [SrO] layers alternating along the stacking axis with *m* [AO_2] layers. Then a simple notation, based on the cation indices (*n* - 1)2(*m* - 1)*m*, has been adopted by the community to denote these materials. For A = Fe, in the iron rich part of the Sr – Fe – O, the incommensurate modulated phase $Sr_4Fe_6O_{13-\delta}$, was structurally analyzed in detail by single

crystal X-ray diffraction and the results led to the formulation $(Fe_2)(Sr_2)FeO_{6.5-\delta/2}$ (n = 3, m = 1), which highlights the particularity of the double intermediate layer in the RS block to contain only transition metals (instead of $5d^{10}$ cations in the HTSCs)[1]. The second member of the iron-rich strontium oxides family (n = 3, m = 2) was obtained by substituting Sr^{2+} with Bi^{3+} and the formalism used to describe its structure is $(Fe_2)(Bi_{0.69}Sr_{1.31})SrFe_2O_{9.5\pm1/2\delta}$ [2]. Thus these first two members were denoted Fe-2201 and Fe_{Bi}-2212 respectively, in order to outline the structural difference with the other Bi-2201 or Bi 2212 structures in the Bi-rich Bi – Sr – Fe – O system. In 2008 a third member of this iron-rich family was isolated, and its preliminary structural characterization highlighted a first schematic representation of the structural model in accordance with electron diffraction (ED) studies and High Resolution Transmission Electron Microscopy (HRTEM) and Z-contrast imaging observations. This schematic model led to the formulation $(Fe_2)(Sr_2)(Sr_3)Fe_4O_{14.65}$ (n = 3, m = 4)[3], and then can be named Fe-2234. Attempts to synthesize single crystal of this phase for solving the structure by single crystal X-ray diffraction have been unsuccessful, and solving the structure ab-initio by powder X-ray diffraction is almost impossible due to the numerous diffraction peaks. In the present article we propose to solve the structure of this phase using tools provided by electron crystallography, in order to highlight structural details like oxygen positions. Different methods have been developed these past few years to collect three dimensional electron diffraction data : zone axis Precession Electron Diffraction (PED) [4-12], Electron diffraction tomography (EDT)[13 – 22,27] and Rotation Electron Diffraction (RED) [23-26]. The advantage of all these techniques is to solve structures analogously to conventional single crystal X-ray diffraction, on micro or nano-sized particles present in a powder, which is particularly interesting in the case of multiphased samples. Solving structures from electron diffraction data is a quite recent science, but numerous structures have already been solved, including complex structures presenting incommensurate modulation[27] or containing light cations like Li^{+}[11,12].

In the present work, manual electron diffraction tomography was the technique used for solving the structure of $Sr_5Fe_6O_{15.4}$ (Fe-2234). The resulting structural model was refined from powder X-ray diffraction data.

2. Experimental section

For the TEM observations the black powder sample was synthesized by conventional solid state reaction[3]. The specimen for Transmission Electron Microscopy (TEM) analysis was prepared by crushing a small part of the pellet in an agate mortar containing ethanol, and a drop of the suspension was deposited on a copper grid covered with a holey carbon film. Electron diffraction patterns were recorded using a 4k × 4k CMOS-TVIPS TEM camera with a 16 bits dynamic range, and the Energy Dispersive Spectroscopy (EDS) analysis was performed using a Brüker Silicon Drift Detector. Zone Axis Selected Area Diffraction (SAED) was performed with a LaB_6 Philips CM300ST transmission electron microscope operating at 300kV, equipped with a

±30° double tilt sample holder. Manual electron diffraction tomography was performed using a single tilt tomography sample holder with a tilt range from -60° to +49°. The dataset was collected by recording an ED pattern each time the sample holder was manually 1° tilted. A precession angle of 1.2° was applied to integrate the whole intensity of the reciprocal space rods. Then the dataset were processed using PETS program[28]. The program performs peak extraction on each ED pattern, and then refines the azimuthal angle between the horizontal axis and the projection of the tilt axis. After having analyzed the peak positions, PETS performs a difference vector space analysis to produce a complete representation of the reciprocal space. The program JANA2006[29] was used as a graphical interface to find the unit cell and to refine the orientation matrix that allows integrating the reflection intensities of each ED pattern by PETS. Intensities belonging to the same reflection on adjacent patterns are integrated together, and the final list of intensities contains one value per each hkl indices with the corresponding estimated standard deviation[30]. Thus the resulting intensity file was used as an input for ab initio structure determination by direct methods with the software SIR2011, which contains special algorithms adapted to Electron Diffraction[13,31].

Powder X-ray diffraction (XRD) pattern was recorded on a D8 ENDEAVOR diffractometer in reflection mode using Cu K_α radiation ($\bar{\lambda}$ = 1.54181 Å), in the range $10° \leq 2\theta \leq 100°$ with 0.02° stepsize. The structure was refined by the Rietveld method using FULLPROF SUITE program[32] integrated in WINPLOTR software[33].

3. Results

3-1. Crystal structure determination The EDS analysis, performed on over 40 particles of the phase, exhibits a ratio Sr/Fe ≈ 0.80±0.04. By tilting around crystallographic axes, SAED patterns were recorded for reciprocal space reconstruction, and the three main zone axes [100], [010] and [001] are presented as example in Fig. 1(a), 1(b) and 1(c). The reciprocal space reconstruction highlighted an orthorhombic unit-cell, defined by the cell parameters a ≈ 27 Å, b ≈ 5.4 Å and c ≈ 42.5 Å. The systematic extinction conditions on hkl reflections are h+k = 2n, k+l = 2n, h+l = 2n simultaneously, which are consistent with a F lattice type (Fig. 1(d), 1(e)). No other extra extinction conditions have been revealed, and then the possible space groups are *Fmmm*, *Fmm2*, *Fm2m*, *F2mm* or *F222*. This unit cell was confirmed by the cell determination in JANA2006 from electron diffraction tomography dataset.

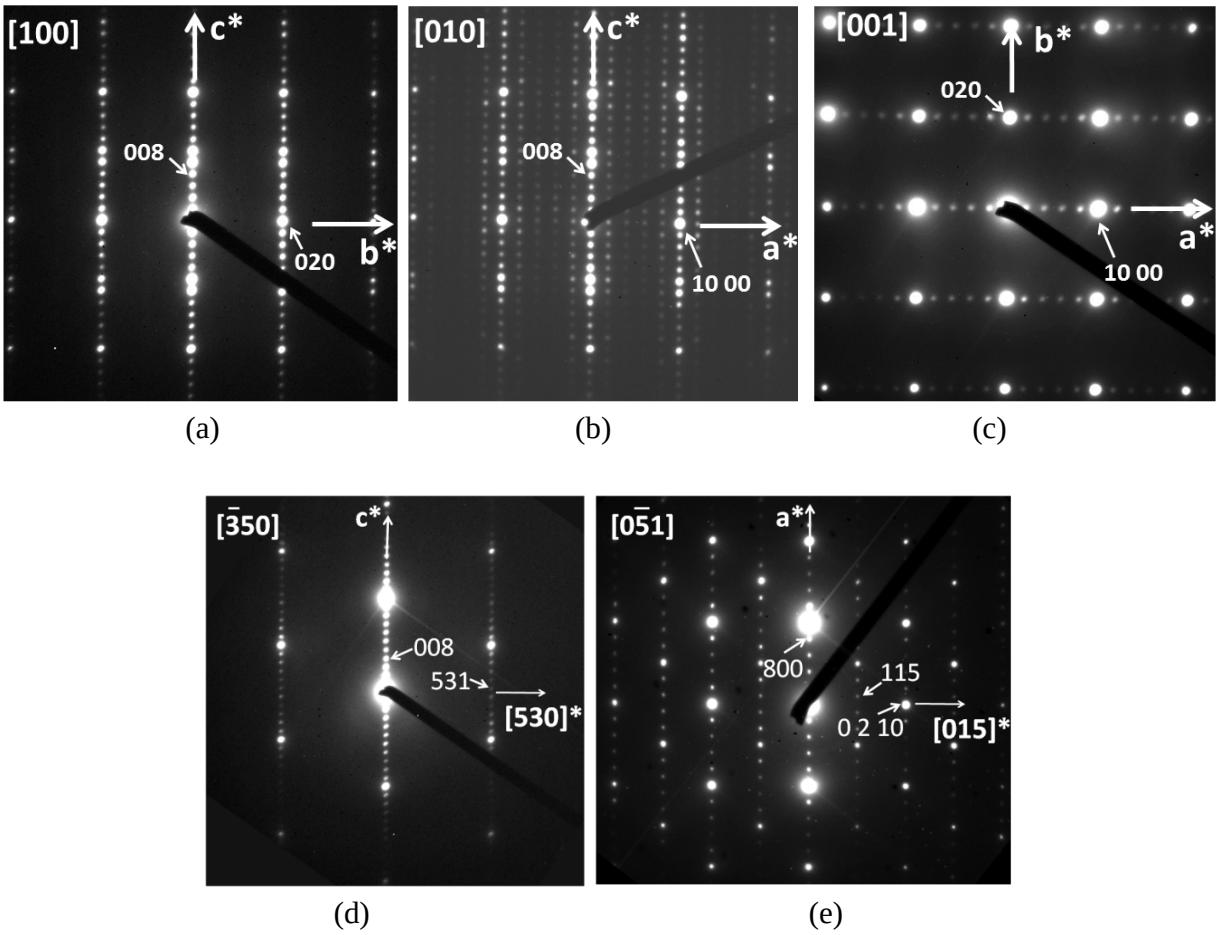

Fig. 1. (a) [100], (b) [010], (c) [001], [$\bar{3}$50] and [0$\bar{5}$1] SAED patterns. All patterns are indexed in the *F*-lattice type orthorhombic unit cell.

The structure resolution was performed by SIR2011 software using the direct methods. The input file contains the following informations :

- The cell parameters : cell parameters determined from electron diffraction being much less accurate than those from powder X-ray diffraction, the cell parameters refined by Lebail refinement on powder X-ray diffraction data were used :

- The possible space groups to test : *Fmmm*, *Fmm2*, *Fm2m*, *F2mm or F222*.

- The nominal composition : 100Sr 120Fe 280O obtained by a simple proportional calculation between the number of atoms in $Fe_2(Bi_{0.69}Sr_{1.31})SrFe_2O_{9.33}$ (Fe_{Bi}-2212, V = 2498 Å^3) and the number of atoms in our unit cell (Fe-2234, V = 6426 Å^3).

- The resolution $d_{resolution}$: radius of a sphere containing the number of reflections taken into account for structure determination. Calculations were made for $d_{resolution}$ = 0.8 Å.

- The two-beam approximation of dynamical theory $I_{hkl} \propto |F_{hkl}|$: amplitudes of diffracted beams are comparable to the amplitude of the incident beam. Two-beam approach assumes that only the incident and the diffracted beams interact in the crystal.

First trials for solving the structure were carried out using the highest symmetry space group *Fmmm*. Among the 14755 measured reflections, 1746 reflections were retained with $I > 3\sigma$; leading to R_{int} of 34 and a redundancy of 3.6. After SIR2011 calculations, 1020 independent reflections were taken into account for a $d_{resolution}$ of 0.8 Å, giving rise to a completeness of 58 %. The output of the direct method calculations is a density map that is interpreted as atomic positions by SIR2011. The structure solution model is presented in Fig. 2 (a), and can be described as a regular alternation of Sr rows with Fe rows along c axis, with however two successive Fe rows at $0.2 < z < 0.3$ and $0.7 < z < 0.8$. The model clearly shows a lack of oxygen atoms since only 128 oxygens among the 280 expected are present. This observation is explained by the [010] oriented electron density map in Fig. 2(b) where no electrostatic potential maxima is found around the double Fe layer at $0.20 < z < 0.30$, and very few electron density maxima around Fe rows sandwiched between two Sr rows. Clearly, oxygen atoms are weakly detected.

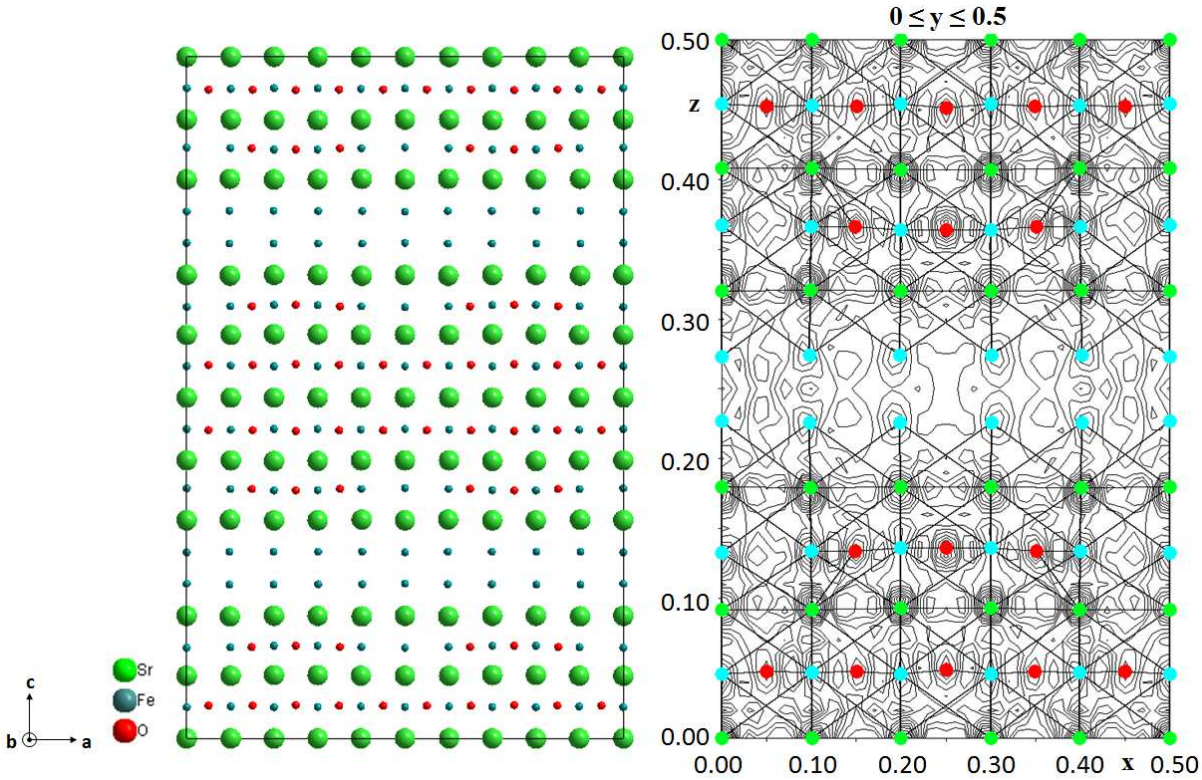

(a) (b)

Fig. 2. (a) [010] projection of the structure model obtained in *Fmmm* at $d_{resolution}$ = 0.8 Å, (b) [010] projection of the electron density map generated by SIR2011 in *Fmmm* after direct method calculations. For better viewing, only 1/8 of the unit cell is represented for $0 \leq y \leq 0.5$. Sr (in green), Fe (in blue) and O (in red) atoms are superimposed on it.

Other trials in ab-initio structure resolution were carried out using a lower symmetry, by replacing one of the m mirror by a 2-fold axis. The position of the 2-fold axis was chosen identical to the one of the parent compound Fe_{Bi}-2212, which is along b axis[2]. In *Fm2m* space group, 1737 reflections were retained for $I > 3\sigma$, leading to a R_{int} of 32.5 and a redundancy of 2.1. The [010] projection of the 3D electron density map generated by VESTA after SIR2011 calculations is presented in Fig. 3(a), and its interpretation by SIR2011 in term of atomic positions is presented in Fig. 3(b). As observed on both figures the cationic arrangement remains the same as the one in *Fmmm*, consisting of a regular alternation along c axis between Sr rows and Fe rows, with replacement of Sr by Fe at z = 3/11 and z = 17/22, creating double Fe layers. The oxygen atoms are more numerous in *Fm2m* than in *Fmmm*, and they are positioned in a regular way around Sr and Fe atoms in the unit cell. At a first glance, most of oxygen atoms look correctly positioned, but some anomalies are visible, like some oxygen atoms with distances O-O below 1.5 Å (pointed out by black arrows in Fig.3(b)) or absent-oxygen areas (circled dashed line in Fig.3(b)) whereas electron densities are observable on this equivalent areas on the electron density map (circled dashed line in Fig.3(a)). To confirm the goodness of present oxygen positions in the structure and determine missing oxygen atoms in the areas mentioned above, sections of observed Fourier map were created.

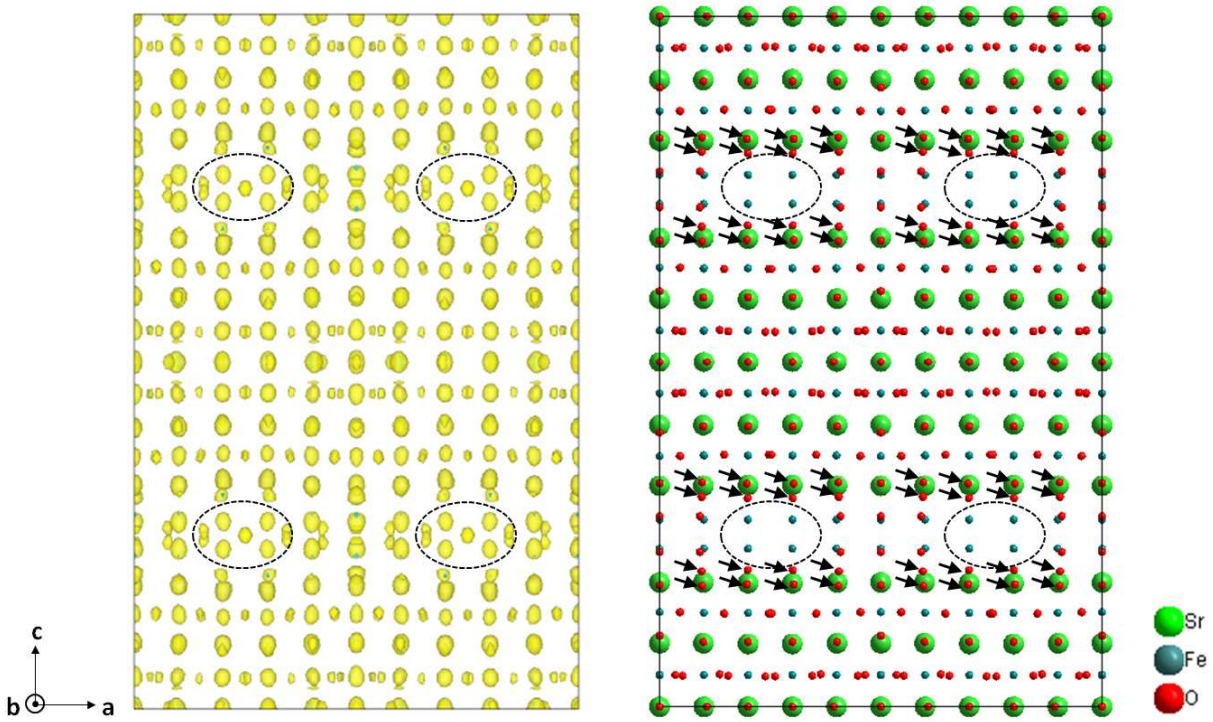

(a) (b)

Fig. 3. (a) [010] projection of the 3D electron density map generated by VESTA after SIR2011 calculations in *Fm2m* space group, (b) Raw structural model as an interpretation by SIR2011 of the electron density map.

In Fig. 4, four sections are presented in the area of the unit cell where Sr and Fe rows alternate regularly along c axis, which corresponds to $0.30 \leq z \leq 0.70$. In Fig. 4(b), the strong electron densities with the electrostatic potential maxima around 36 e.Å^{-1} are attributed to Sr atoms, and those with the maxima around 24 e.Å^{-1} are attributed to Fe atoms (electrostatic potential values were calculated from the mathematical expression established by *Cinthia Corrêa* and *Lukas Palatinus* : U (e.Å^{-1}) = 3.32367(Å)× |e|ρ_{JANA}(r)(Å^{-2}), with e = electron charge and ρ_{JANA}(r) = electrostatic potential given by JANA2006). The three other sections in Fig. 4(a), 4(c) and 4(d) exhibit electron densities with electrostatic potential maxima around 10 e.Å^{-1}, corresponding to O atoms. Those at y = 0.05 (Fig. 4(a)) and y = 0.554 (Fig. 4(d)) are situated at the same z level as Fe atoms (Fig. 4(b)), surrounding them to form square plane environments, and O atoms at y = 0.356 (Fig. 4(c)) are positioned at the top and bottom of each Fe atoms. For instance Fe3 in Fig. 4(b) (highlighted in red) is surrounded by O13/O14 of Fig. 4(a) with Fe-O distances of 1.82 Å and 1.87 Å respectively, O12/O13 of Fig. 4(d) with Fe-O distances of 2.08 Å and 2.08 Å respectively, and O3/O17 of Fig. 4(c) with Fe-O distances of 2.07 Å and 2.15 Å. So we can deduce that all Fe atoms in the slab of the unit cell at $0.3 \leq z \leq 0.7$ are in octahedral environments, with Sr atoms positioned in between, which finally describes a quadruple perovskite-type layer.

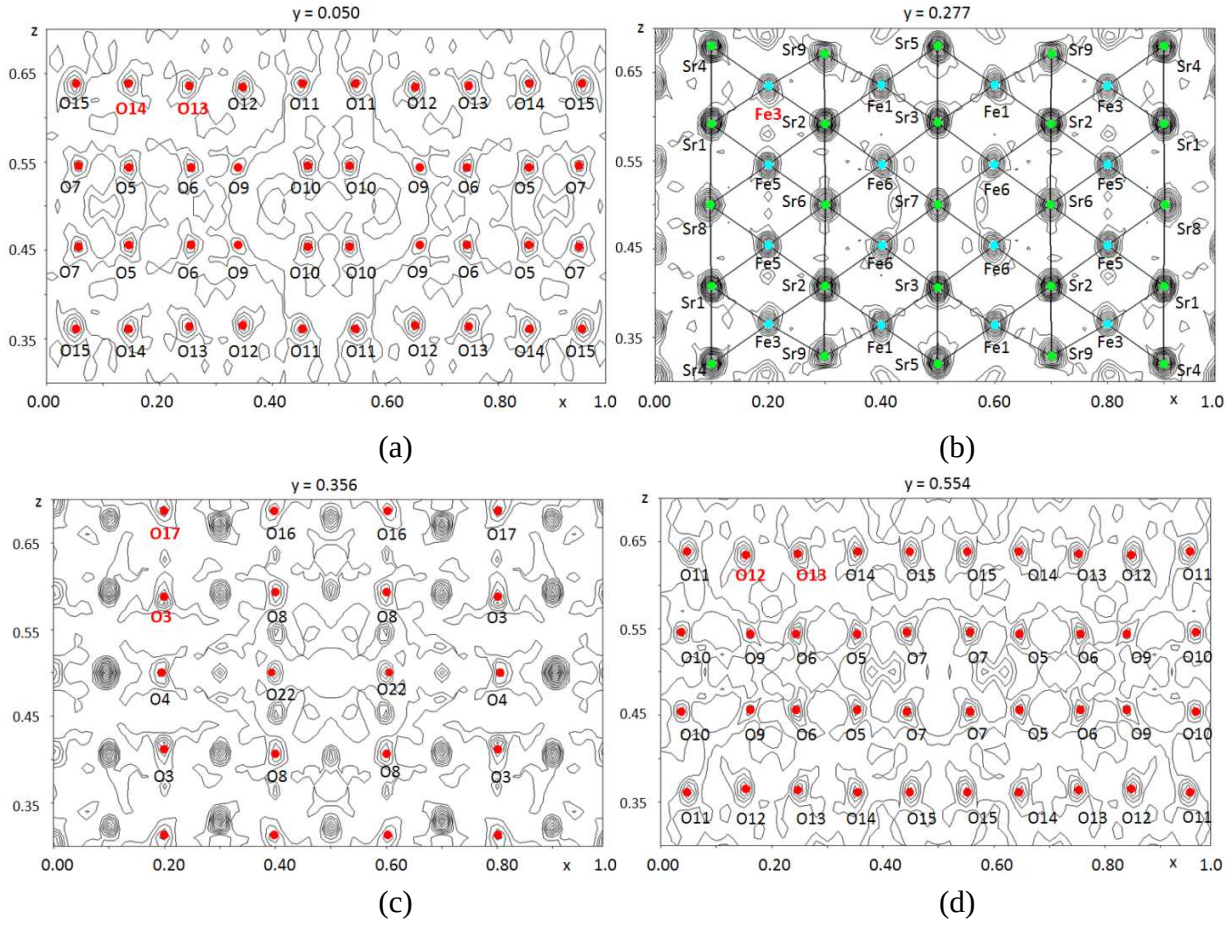

Fig. 4. [010] observed Fourier map sections at (a) y = 0.05, (b) y = 0.277, (c) y = 0.356 and (d) y = 0.554. They all exhibit electron densities corresponding to Sr, Fe and O in the part of the unit cell included between z = 0.30 and z = 0.70.

Now we will interest to the slab of the unit cell with the double Fe layer ($0.21 \leq z \leq 0.29$). According to the raw structural model in Fig. 3(b), some oxygen atoms were missing in this area. Sections at y = 0.05 (Fig. 5(a)) and y = 0.40 (Fig. 5(c)) allowed to determine these oxygen positions by identifying electron densities whose electrostatic potential maxima were above 10 $e.Å^{-1}$ on the one hand, and on the second hand with reasonable distances (around 2 Å) between them and Fe atoms present at the section y = 0.02 (Fig. 5(b)). The resulting determined oxygen atoms were O18 (Fig. 5(a), electrostatic potential maxima = 13 $e.Å^{-1}$, $d_{O18\text{-}Fe9}$ = 1.8 Å) and O20 (Fig. 5(c), electrostatic potential maxima = 11.6 $e.Å^{-1}$, $d_{O20\text{-}Fe9}$ = 1.9 Å, $d_{O20\text{-}Fe9}$ = 2.2 Å and $d_{O20\text{-}Fe7}$ = 1.9 Å). A slight shift of O19 and O23 positions was applied in order to fit better with the maxima of the electron densities. The atomic arrangement between oxygen and iron atoms is presented in Fig.5 (d) and Fig. 5(e) in the range of y = 0.05 to y = 0.4 and y = 0.05 to y = 0.9 respectively. The arrangement in this slab is very analogous to the double rock-salt type layer observed in intergrowth type structures called Bi-22(m-1)m, with Fe atoms instead of Bi in the double layer, reducing thus the distance between the two layers and conferring larger displacements of oxygen atoms, in such a way that an extra oxygen O18 is periodically inserted every 5 Fe atoms along a axis between the two Fe layers. These structural features were already highlighted in the phases called Fe-2201 and Fe_{Bi}-2212, confirming the belonging of our phase to this family of layered iron oxides.

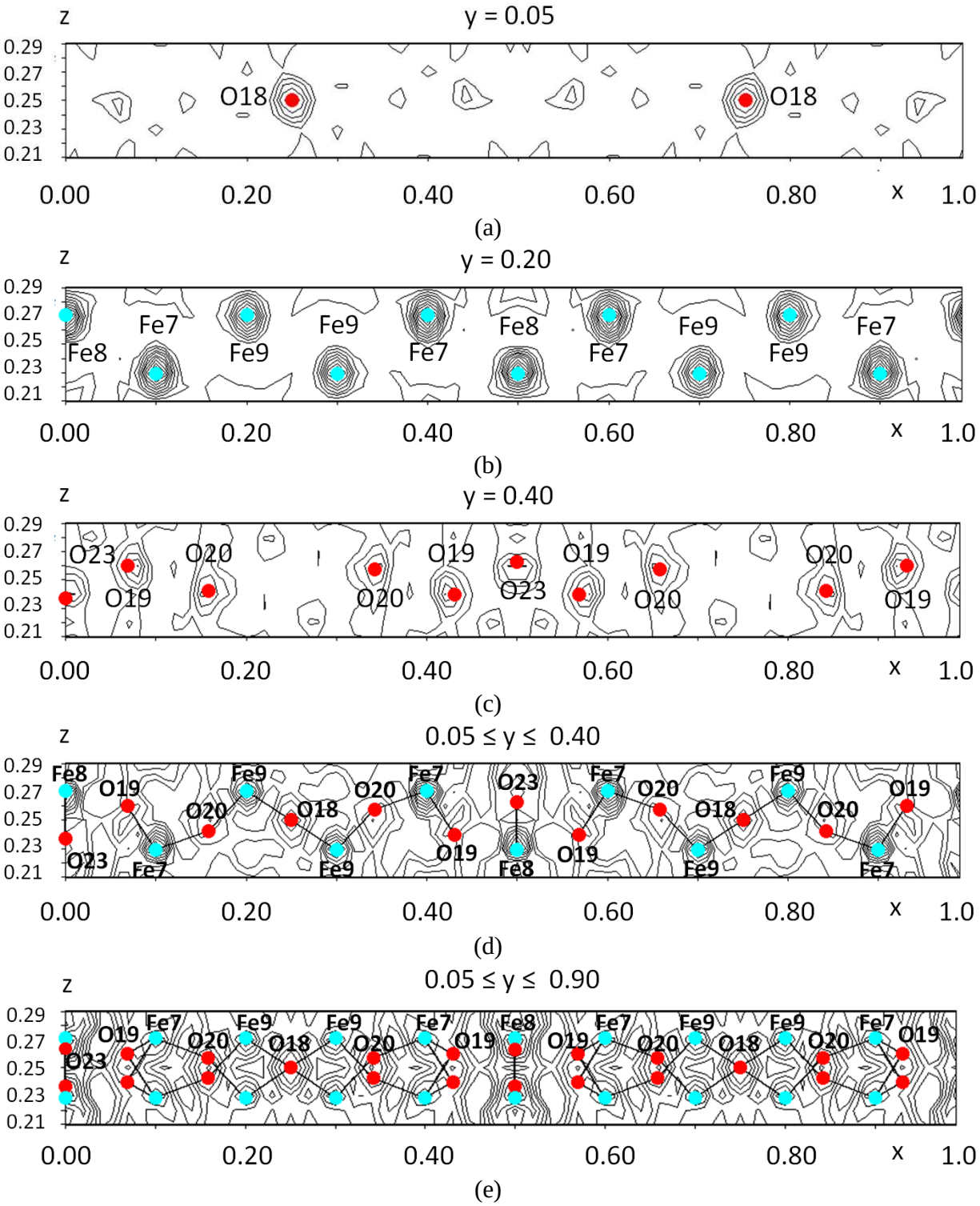

Fig. 5. [010] observed Fourier map sections at (a) y = 0.05, (b) y = 0.20, (c) y = 0.40, (d) $0.05 \leq y \leq 0.40$ and (e) $0.05 \leq y \leq 0.90$. They all exhibit electron densities for Fe and O in the part of the unit cell included between z = 0.21 and z = 0.29.

3-2. Structure refinement

The *Fm2m* space group and the atomic positions calculated by the direct methods on SIR2011 were used as starting sets in the refinement procedure. 24 points were picked up on the experimental diagram to create the background, while the diffraction peaks were fitted using a pseudo-voigt function. The half width parameter of the diffraction peaks was evaluated by the Caglioti equation[34]. The cell parameters and atomic positions of the secondary phase $SrFe_{12}O_{19}$ have been considered and refined in order to index correctly the whole set of diffraction peaks on the diagram. After this refinement, all parameters of this phase were fixed and the cell parameters of the phase Fe-2234 as well as the profile function parameters were refined. Then the scale factor and the cationic positions were refined. Considering the high number of independent atomic positions in the structure, the fact that the structure to refined is one of two phases present in the powder and the fact that oxygen is poorly visible by X-rays, it is clear that refinement of oxygen positions is rather irrelevant. So to maintain stable the oxygen positions during the Rietveld refinement, restrain in cation-oxygen distances was applied and cation positions were fixed, with application of a low damping factor. The refinement led to satisfactory reliability factors as well as a good agreement between the experimental and calculated XRD diagrams. Details of the refinement conditions, cell parameters, phase contents and reliability factors are given in Table 1. Atomic positions are given in Tables 2 and in supporting information with the interatomic bond distances. The observed and calculated XRD diagrams with their difference curve are presented in Fig. 6 displaying a good agreement between observed and calculated diffraction profiles. The final structure, presented in Fig. 7(a) (with atoms) and Fig. 7(b) (with polyhedra), is described as a stacking of a quadruple perovskite-type layer with a double rock-salt type layer, where the sequence of polyhedra along a axis consists of three corner-sharing tetrahedra (in yellow) linked by the corner with one distorted tetragonal pyramids (in green). The chemical formula per unit cell is $Sr_{100}Fe_{120}O_{308}$, which is reduced to $Sr_5Fe_6O_{15.4}$.

Results obtained from Rietveld's profile analysis method	
Step scan increment (°2θ)	0.02
2θ range (°)	10 -100
phase 1 : $Sr_5Fe_6O_{15.4}$ (space group F m2m/Z = 20)	
scale factor	0.0000188(1)
U	-0.0105(18)
V	0.0239(17)
W	-0.00144(34)
shape	0.17(1)
a(Å)	27.4047(3)
b(Å)	5.48590(7)
c(Å)	42.7442(4)
V(Å^3)	6426.14(13)
phase content(%)	56.25(22)
Rbragg (%)	18.5
phase 2 : $SrFe_{12}O_{19}$ (space group P 6_3/mmc/Z = 2)	
scale factor	0.0000360(3)
U	0.0217(5)
V	-0.003(5)
W	0.005(1)
shape	0.09(2)
a(Å)	5.88618(4)
c(Å)	23.0540(3)
V(Å^3)	691.742(12)
phase content(%)	43.75(26)
Rbragg (%)	15.8
global χ^2(%)	2.57

Table 1. Parameters and reliability factors obtained by the Rietveld refinement of the powder X-ray diffraction diagram containing both phases $Sr_5Fe_6O_{15.4}$ (Fe-2234) and $SrFe_{12}O_{19}$.

	Wyckoff	x	y	z		Wyckoff	x	y	z
Sr1	16e	0.1004(18)	0.2818(27)	0.4082(8)	O4	8d	0.1951(71)	0.3270(16)	0.5
Sr2	16e	0.2006(13)	0.7742(33)	0.4085(13)	O5	16e	0.1463(82)	0.0829(73)	0.456(5)
Sr3	8c	0	0.7662(17)	0.4072(8)	O6	16e	0.2558(95)	0.0829(19)	0.4561(51)
Sr4	16e	0.1011(18)	0.2655(23)	0.3198(6)	O7	16e	0.0570(82)	0.0939(96)	0.4541(45)
Sr5	8c	0	0.7650(28)	0.3199(11)	O8	16e	0.0998(7)	0.8511(82)	0.4069(51)
Sr6	8d	0.1992(11)	0.7590(17)	0.5	O9	16e	0.1612(53)	0.5620(74)	0.4560(50)
Sr7	4a	0	0.7460(23)	0.5	O10	16e	0.0370(89)	0.5523(35)	0.4539(43)
Sr8	8d	0.0982(13)	0.2979(14)	0.5	O11	16e	0.4528(53)	0.0511(7)	0.3612(62)
Sr9	16e	0.2008(13)	0.3010(12)	0.1709(8)	O12	16e	0.3472(81)	0.0498(7)	0.3651(47)
Fe1	16e	0.1006(15)	0.7563(40)	0.3641(19)	O13	16e	0.7470(75)	0.0505(85)	0.3638(55)
Fe2	8c	0	0.2548(15)	0.3632(12)	O14	16e	0.8552(86)	0.0505(91)	0.3612(44)
Fe3	16e	0.1997(17)	0.2510(29)	0.3650(13)	O15	16e	0.0520(52)	0.0505(11)	0.3612(44)
Fe4	8c	0	0.2344(21)	0.4540(12)	O16	16e	0.3678(60)	0.3487(88)	0.3132(48)
Fe5	16e	0.1985(20)	0.2428(52)	0.4539(18)	O17	16e	0.1991(84)	0.3514(75)	0.3132(43)
Fe6	16e	0.0990(22)	0.7550(35)	0.4540(13)	O18	8b	0.75	0.0699(43)	0.25
Fe7	16e	0.1021(23)	0.7180(31)	0.2710(12)	O19	16e	0.0691(59)	0.4106(29)	0.2599(46)
Fe8	8c	0	0.2157(19)	0.2710(11)	O20	16e	0.1580(51)	0.3798(83)	0.2426(40)
Fe9	16e	0.1999(24)	0.2151(42)	0.2709(17)	O21	8c	0	0.7887(78)	0.1888(70)
O1	4a	0	0.3130(44)	0.5	O22	8d	0.4140(64)	0.25	0.5
O2	8c	0	0.3391(17)	0.4081(48)	O23	8c	0.5	0.4018(85)	0.2631(40)
O3	16e	0.1991(82)	0.3451(92)	0.4122(45)					

Table 2. Atomic positions in $Sr_5Fe_6O_{15.4}$ (Fe-2234) after powder X-ray diffraction refinement.

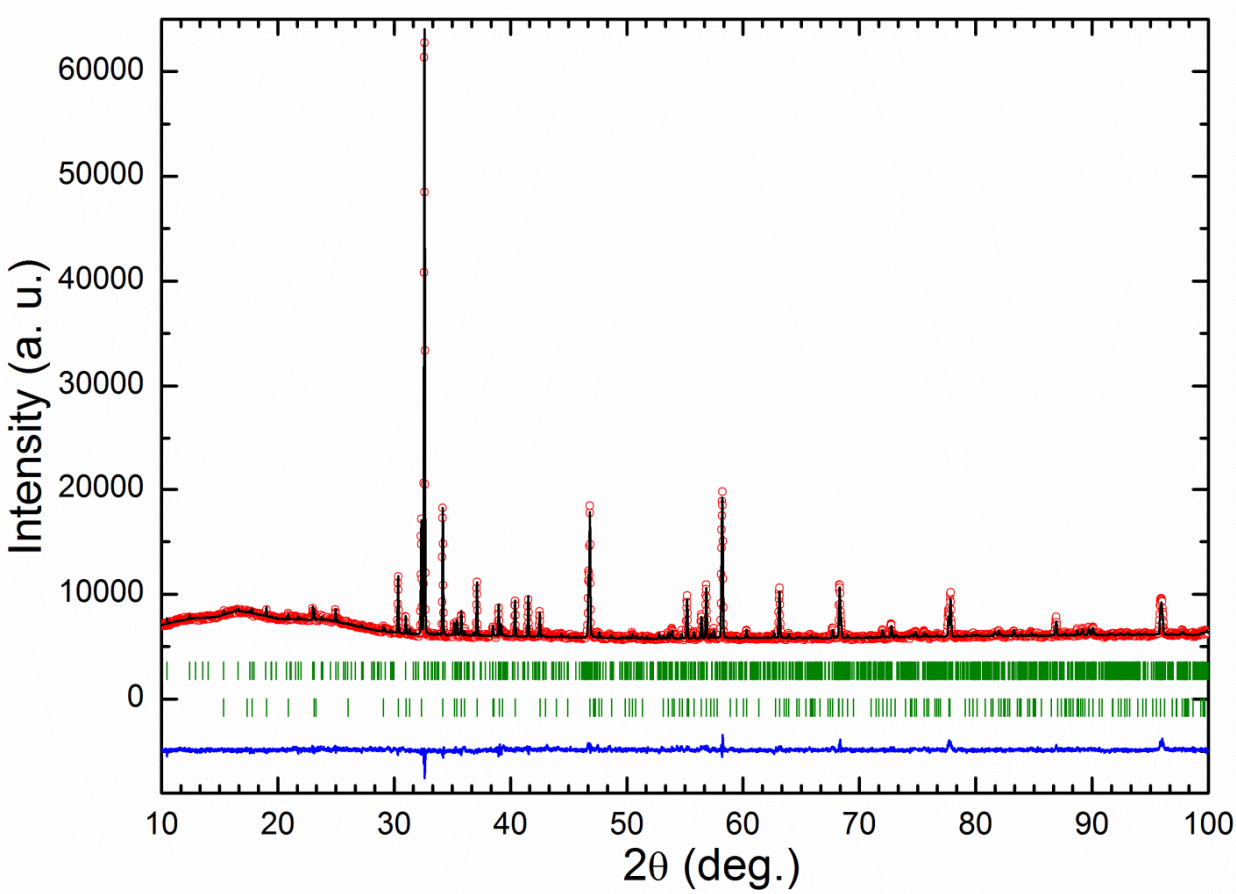

Fig. 6. Final plot of the Rietveld refinement, showing the experimental (red circles), calculated (black line) and difference (blue line) curves in the range 2θ = 10° - 100°. Green vertical markers refer to the calculated positions of the Bragg reflections for $Sr_5Fe_6O_{15.4}$ and $SrFe_{12}O_{19}$ respectively.

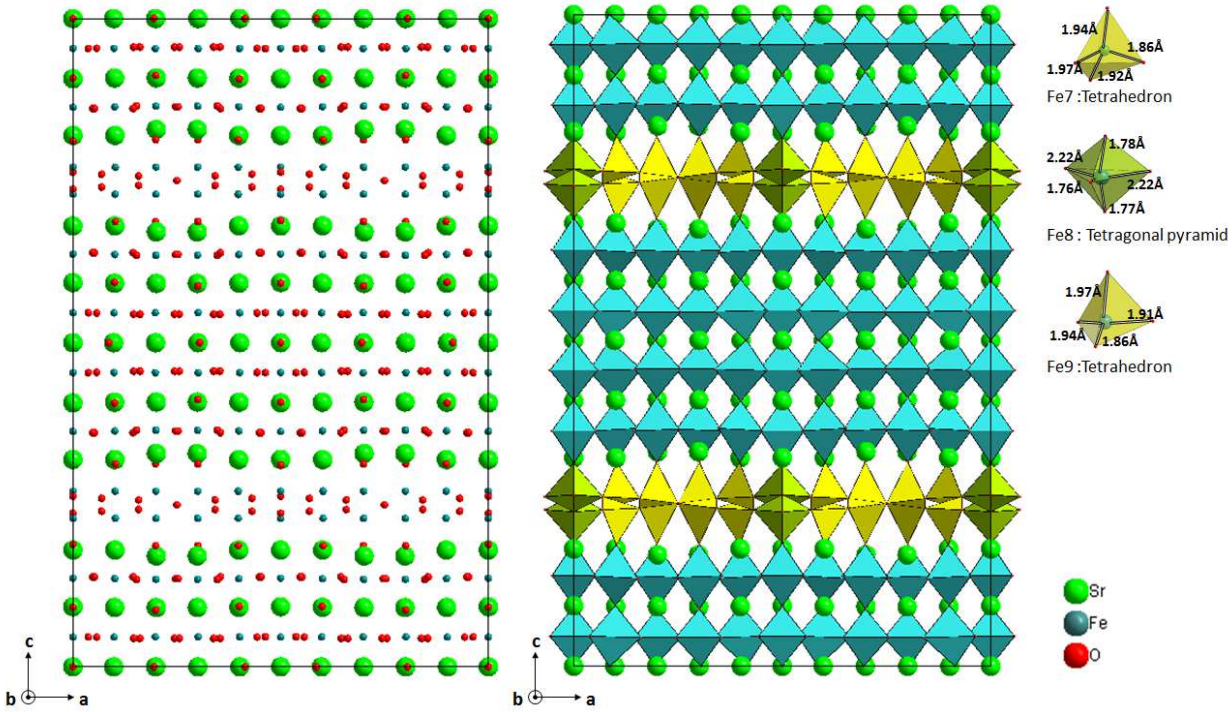

(a) (b)

Fig. 7. Schematical representation of the refined structure projected along b axis (a) without coordination polyhedra and (b) with coordination polyhedra.

4. Conclusion-Discussion

The crystal structure of $Sr_5Fe_6O_{15.4}$ has been successfully solved by electron diffraction tomography combined with powder X-ray diffraction refinement by Rietveld method. The direct methods applied on the electron tomography dataset were perfectly suitable to determine the structure model in *Fm2m* space group with correct detection of all the cation and oxygen positions. This structure is described as a stacking along c axis of a quadruple perovskite-type layer composed of Fe distorted octahedra, with a Fe double row similar to a double rock-salt type layer where iron is found in tetrahedral and tetragonal environments. This structure is comparable to the parent structures $Fe_2Sr_2FeO_{6.5-\delta/2}$ (Fe-2201) and $Fe_2(Bi_{0.69}Sr_{1.31})SrFe_2O_{9.33}$ (Fe_{Bi}-2212), both solved on single crystal X-ray diffraction some years ago and consisting of the alternation of single or double perovskite layer with a similar Fe-double row..

The substitution of Sr^{2+} by Bi^{3+} in Fe-2201 led to a double perovskite-type layer in the phase Fe_{Bi}-2212 by adding more oxygen. Its structural analysis by single crystal X-ray diffraction demonstrated that Bi atoms were situated at the periphery of the double perovskite-type layer. In our phase Fe-2234, the quadruple perovskite-type layer is not a consequence of strontium substitution by a trivalent cation, but is due to a Fe^{3+}/Fe^{4+} mixed valence state of iron, which was

confirmed by Mössbauer study in a previous work[3]. If we consider Fe^{4+} cations present in the first and fourth layer of the quadruple perovskite-type layer, in a same way as bismuth is present at the periphery of the double perovskite-type layer in Fe_{Bi}-2212, these irons refer to Fe1 (position 16e), Fe2 (position 8c) and Fe3 (position 16e), which leads to 40 iron cations in 4+ valence state and then the 80 remaining iron cations are 3+. By a consequence the number of oxygen atoms in the structure is reduced to 300 per unit cell, involving 8 oxygen vacancies in the structure, and so the deletion of one oxygen position with multiplicity 8 is needed. Among all the oxygen positions with this multiplicity, the most relevant to remove is O22, in 8d Wyckoff site since the oxygen vacancies are situated in the middle of the quadruple perovskite-type layer (Fig.8). This hypothesis of structure with oxygen vacancies is important to consider since their presence would bring more relaxation in the structure and therefore reduce the polyhedra distortions. Obviously this hypothesis is impossible to verify by a structure refinement from powder X-ray diffraction, only refinement from neutron diffraction data could confirmed the presence or not of these oxygen vacancies.

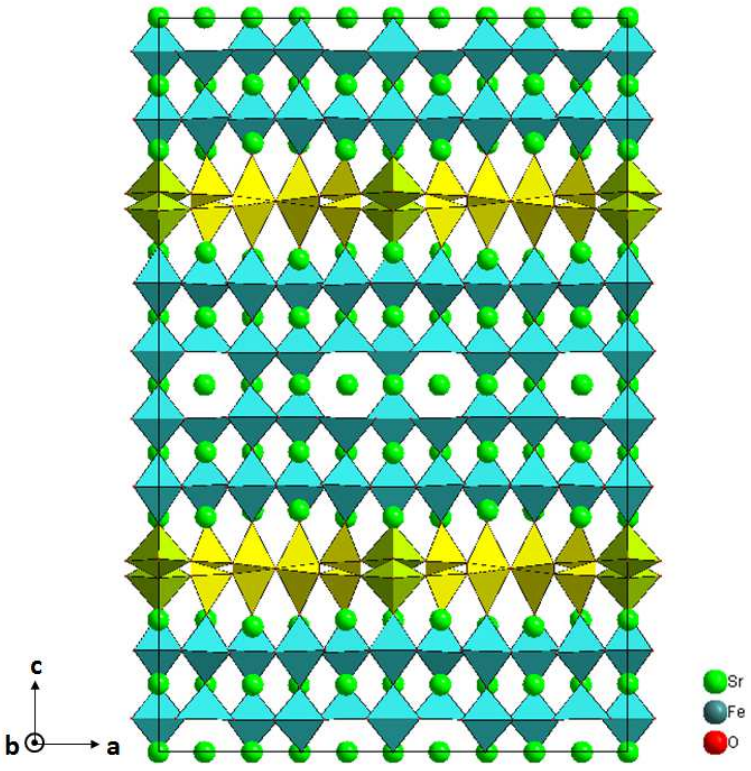

Fig. 8. [010] schematical representation of the Fe-2234 structure with the hypothesis of oxygen vacancies in the middle of the quadruple perovskite-type layer. The chemical formula becomes $Sr_5Fe_6O_{15}$.

ACKNOWLEDGMENTS

The author thanks Dr. Olivier Leynaud for his help in Rietveld refinements on powder XRD. The author thanks also Pr. Sylvie Malo and Pr. Maryvonne Hervieu (CRISMAT, Caen) for providing a piece of sample.

REFERENCES

(1) Pérez, O.; Mellenne, B.; Retoux, R.; Raveau, B.; Hervieu, M. A new light on the iron coordination in $Sr_4Fe_6O_{13\pm\delta}$: Super space formalism and structural mechanism. *Solid State Sci.* **2006**, *8*, 431−443.

(2) Grebille, D. ; Lepoittevin, C.; Malo, S.; Pérez, O.; Nguyen, N.; Hervieu, M. Disordered commensurate structure of the 2212-related phase $Fe_2(Bi_{0.69}Sr_{2.31})Fe_2O_{9.5\pm1/2\delta}$ and structural mechanism. *J. Solid State Chem.* **2006**, *179*, 3849−3859.

(3) Lepoittevin, C.; Malo, S.; Nguyen, N.; Hebert, S.; Van Tendeloo, G.; Hervieu, M. A Layered Iron-Rich 2234-Type with a Mixed Valence of Iron: The Ferrimagnetic Tl-doped $Fe_2(Sr_{2-\varepsilon}Tl_\varepsilon)Sr_3Fe_4O_{14.65}$. *Chem. Mater.* **2008**, *20*, 6468−6476.

(4) Gjønnes, J.; Hansen, V.; Berg, B.S.; Runde, P.; Cheng, Y.F.; Gjønnes, K.; Dorcet, D.L.; Gilmore, C.J. Structure Model for the Phase Al_mFe Derived from Three-Dimensional Electron Diffraction Intensity Data Collected by a Precession Technique. Comparison with Convergent-Beam Diffraction. *Acta Cryst. Sect. A : Found. Crystallogr.* **1998**, *54*, 306−319.

(5) Boulahya, K.; Ruiz-González, L.; Parras, M.; González-Calbet, J.M.; Nickolsky, M.S.; Nicolopoulos, S. Ab initio determination of heavy oxide perovskite related structures from precession electron diffraction data. *Ultramicroscopy* **2007**, *107*, 445−452.

(6) Novitskaya, M.; Makhnach, L.; Ivashkevich, L.; Pankov, V.; Klein, H.; Rageau, A.; David, J.; Gemmi, M.; Hadermann, J.; Strobel, P. Synthesis, crystal structure and physico-chemical properties of the new quaternary oxide $Sr_5BiNi_2O_{9.6}$. *J. Solid State Chem.* **2011**, *184*, 3262−3268.

(7) Dorset, D.L.; Gilmore, C.J.; Jorda, J.L.; Nicolopoulos, S. Direct electron crystallographic determination of zeolite zonal structures. *Ultramicroscopy* **2007**, *107*, 462−473.

(8) Gemmi, M.; Nicolopoulos, S. Structure solution with three-dimensional sets of precessed electron diffraction intensities. *Ultramicroscopy* **2007**, *107*, 483−494.

(9) Klein, H. Precession electron diffraction of Mn_2O_3 and $PbMnO_{2.75}$: solving structures where X-rays fail. *Acta Cryst. Sect. A : Found. Crystallogr.* **2011**, *67*, 303−309.

(10) Boullay, P.; Dorcet, V.; Pérez, O.; Grygiel, C.; Prellier, W.; Mercey, B.; Hervieu, M. Structure determination of a brownmillerite $Ca_2Co_2O_5$ thin film by precession electron diffraction. *Phys. Rev. B : Condens. Matter* **2009**, *79*, 184108.

(11) Gemmi, M.; Klein, H.; Rageau, A.; Strobel, P.; Le Cras, F. Structure solution of the new titanate $Li_4Ti_8Ni_3O_{21}$ using precession electron diffraction. *Acta Crystallogr., Sect. B: Struct. Sci.* **2010**, *66*, 60−68.

(12) Hadermann, J.;. Abakumov, A.M; Turner, S.; Hafideddine, Z.; Khasanova, N.R.; Antipov, E.V.; Van Tendeloo, G. Solving the Structure of Li Battery Materials with Precession Electron Diffraction: Application to Li_2CoPO_4F. *Chem. Mater.* **2011**, *23*, 3540−3545.

(13) Gemmi, M.; Campostrini, I.; Demartin, F.; Gorelik, T.E.; Gramaccioli, C.M. Structure of the new mineral sarrabusite, $Pb_5CuCl_4(SeO_3)_4$, solved by manual electron-diffraction tomography. *Acta Crystallogr., Sect. B : Struct. Sci*. **2012**, *68*, 15−23.

(14) Klein, H.; David, J. The quality of precession electron diffraction data is higher than necessary for structure solution of unknown crystalline phases. *Acta Cryst. Sect. A : Found. Crystallogr*., **2011**, *67*, 297−302.
(15) Klein, H. Structure solution of oxides from zones axes precession electron diffraction data. *Z. Kristallogr*. **2013**, *228*, 35−42.
(16) Kolb, U.; Gorelik, T.; Kubel, C.; Otten, M.T.; Hubert, D. Towards automated diffraction tomography: Part I—Data acquisition. *Ultramicroscopy* **2007**, *107*, 507−513.
(17) Mugnaioli, E.; Gorelik, T.; Kolb, U. "Ab initio" structure solution from electron diffraction data obtained by a combination of automated diffraction tomography and precession technique. *Ultramicroscopy* **2009**, *109*, 758−765.
(18) Rozhdestvenskaya, I.; Mugnaioli, E.; Czank, M.; Depmeier, W.; Kolb, U.; Reinholdt, A.; Weirich, T. The structure of charoite, $(K,Sr,Ba,Mn)_{15–16}(Ca,Na)_{32}[(Si_{70}(O,OH)_{180})](OH,F)_{4.0}$-$n$$H_2O$, solved by conventional and automated electron diffraction. *Mineral. Mag*. **2010**, *74*, 159−177.
(19) Andrusenko, I.; Mugnaioli, E.; Gorelik, T.E.; Koll, D.; Panthofer, M.; Tremel, W.; Kolb, U. Structure analysis of titanate nanorods by automated electron diffraction tomography. *Acta Crystallogr., Sect. B: Struct. Sci.* **2011**, *67*, 218−225.
(20) Kolb, U.; Gorelik, T.; Otten, M.T. Towards automated diffraction tomography. Part II—Cell parameter determination. *Ultramicroscopy* **2008**, *108*, 763−772.
(21) Kolb, U.; Gorelik, T.; Mugnaioli, E.; Moeck, P.; Hovmöller, S.; Nicolopoulos, S.; Rouvimov, S.; Petkov, V.; Gateshki, M.; Fraundorf, *P*. Electron Crystallography for Materials Research and Quantitative Characterization of Nanostructured Materials, Materials Research Society, *Warrendale* **2009**, 11−23.
(22) Kim, J.G.; Song, K.; Kwon, K.; Hong, K.; Kim, Y.J. Structure analysis of inorganic crystals by energy-filtered precession electron diffraction. *J. Electron Microsc*. **2010**, *59*, 273−283.
(23) Zhang, D.L.; Gruner, D.; Oleynikov, P.; Wan, W.; Hovmöller, S.; Zou, X. Precession electron diffraction using a digital sampling method. *Ultramicroscopy* **2010**, *111*, 47−55.
(24) Yun, Y.; Wan, W.; Rabbani; F.; Su, J.; Xu, H.; Hovmöller, S.; Johnsson, M. ; Zou, X. Phase identification and structure determination from multiphase crystalline powder samples by rotation electron diffraction. *Appl. Cryst*. **2014**, *47*, 2048−2054.
(25) Su, J.; Kapaca, E.; Liu, L ; Georgieva, V.; Wan, W.; Sun, J.; Valtchev, V.; Hovmöller, S.; Zou, X. Structure analysis of zeolites by rotation electron diffraction (RED). *Micropor. Mesopor. Mater*. *Micropor. Mesopor. Mater*. **2014**, *189*, 115−125.
(26) Wan, W.; Sun, J.; Su, J.; Hovmöller, S.; Zou, X. Three-dimensional rotation electron diffraction : software RED for automated data collection and data processing. *J. App. Crystallogr*. **2013**, *46*, 1863-1873.
(27) Boullay, P.; Palatinus, L.; Barrier, N. Precession Electron Diffraction Tomography for Solving Complex Modulated Structures : the case of $Bi_5Nb_3O_{15}$. *Inorg. Chem.*, **2013**, *52*, 6127-6135.
(28) Palatinus, L. PETS-program for analysis electron diffraction data, Institute of Physics of the AS CR: Prague, Czechia, **2011**.

(29) Petříček, V.; Dusek, M.; Palatinus, L. JANA2006: Structure Determination Software Programs; Institute of Physics: Praha, Czech Republic, **2006**.
(30) Palatinus, L.; Corrêa, C.A.; Steciuk, G.; Jacob, D.; Roussel, P.; Boullay, P. ; Klementová, M. ; Gemmi, M. ; Kopeček, J.; Domeneghetti, M.C.; Cámara, F.; Petříček, V. Structure refinement using precession electron diffraction tomography and dynamical diffraction: tests on experimental data. *Acta Crystallogr., Sect. B: Struct. Sci.***2015**, *71*, 740-751.
(31) Cascarano, G.L.; Giacovazzo, C.; Carrozzini, B. Crystal structure solution *via* precession electron diffraction data: The BEA algorithm. *Ultramicroscopy* **2010,** *111*, 56−61.
(32) Rodriguez-Carvajal, J. *FULLPROF suite*, LLB Saclay and LCSIM, Rennes, France, **2003**.
(33) Roisnel, T.; Rodriguez-Carvajal, WinPLOTR: A windows tool for powder diffraction pattern analysis. *J. Mater. Sci. Forum* **2001**, *118*, 378−381.
(34) Caglioti, G.; Paoletti, A.; Ricci, F.P. Choice of collimators for a crystal spectrometer for neutron diffraction. *Nucl. Instrum.* **1958**, *3*, 223−228.